Nano Energy 112 (2023) 108462

Contents lists available at ScienceDirect

Nano Energy

journal homepage: www.elsevier.com/locate/nanoen

Full paper

Tellurium filled carbon nanotubes cathodes for Li-Te batteries with high capacity and long-term cyclability

Shaoqing Rao [a,1], Ruizhe Wu [c,1], Zhu Zhu [b], Jinsong Wu [b,*], Yao Ding [a,*], Liqiang Mai [a,b,**]

[a] School of Materials Science and Engineering, Wuhan University of Technology, Wuhan 430070, PR China
[b] State Key Laboratory of Advanced Technology for Materials Synthesis and Processing, Wuhan University of Technology, Wuhan 430070, PR China
[c] Collaborative Innovation Center for Advanced Organic Chemical Materials Co-constructed by the Province and Ministry, Ministry of Education Key Laboratory for the Synthesis and Application of Organic Functional Molecules, College of Chemistry and Chemical Engineering, Hubei University, Wuhan 430062, PR China

ARTICLE INFO

Keywords:
Li-Te batteries
Carbon nanotubes
Nanoconfinement
Cycling stability

ABSTRACT

Li-Te batteries, compared with traditional lithium-ion batteries and Li-other group VIA elements (including O, S, Se) batteries, have shown overwhelming features of high specific volumetric capacity and superior electrical conductivity. These features make the Li-Te batteries possess great importance in modern portable electronics and electric vehicles with limited battery package size. However, the Achilles' Heel in Li-Te batteries is the huge volume change and inevitable dissolution of polytellurides during cycling. Herein, we synthesize a cathode material based on polycrystalline Te encapsulated in N-doped multiwall carbon nanotubes (Te-filled CNTs) by physical vapor transport (PVT) method. With unique spatial restriction of the CNT hosts, the electrochemically active Te content can be well preserved, and the prepared Te-filled CNTs cathodes deliver a high specific capacity of 590 mAh g^{-1} based on Te content. More importantly, the reaction kinetics and electrochemical reversibility of the cathodes have been significantly improved by using nanoscale cavities (4–6 nm) which stabilize the polytellurides (Li_2Te_n). Meanwhile, a series of *in situ* characterizations are carried out to straightforwardly reveal a two-step discharge/charge mechanism for Te-filled CNTs. In addition, theoretical calculations prove that the encapsulated Te ensure a lower energy barrier for lithiation compared with bare CNT. This work sheds light on the nanoconfinement effect of CNT for improving the utilization and cycling stability of Te based cathodes in Li-Te batteries.

1. Introduction

Nowadays, lithium-ion batteries (LIBs) have been widely used in portable electronic devices and electric vehicles. However, the energy densities of conventional LIBs are limited to ~ 300 Wh kg^{-1}, which cannot meet the increasing demands of miniaturization for batteries. With the utilization of sulfur as the cathode material (theoretical specific capacity of 1672 mAh g^{-1}), the energy densities of lithium-sulfur (Li-S) batteries can be greatly enhanced. In past decades, researchers used porous carbon, metallic materials [1] or metal oxides [2] as host materials to significantly improve its cycling stability, but the intrinsic low electrical conductivity of sulfur (10^{-30} S m^{-1}) and lithium sulfide (10^{-14} S m^{-1}) greatly hinder the broad application of Li-S batteries. Due to the higher electrical conductivity of selenium (10^{-5} S m^{-1}), lithium-selenium (Li-Se) batteries have been developed to increase the power density and cycle life in recent years [3,4]. Additionally, since 2014, tellurium (Te) with a high volumetric capacity (2604 mAh cm^{-3}) have shown great potential as a new cathode material for rechargeable lithium metal batteries, known as Li-Te batteries [5,6]. Specifically, despite the high cost and low abundance of Te, the intrinsic higher electrical conductivity (2×10^2 S m^{-1}) provides higher utilization of active materials and conversion reaction kinetics, which makes Li-Te batteries quite promising in advanced wearable electronics and aerospace applications [7–9].

However, at current stage, Te cathodes encounter the same issue of shuttle effect and volume change as S and Se cathodes, which is detrimental to the cycling stability of Li-Te batteries. One effective strategy is to employ porous carbon as the host of Te [5]. Although many porous

* Corresponding authors.
** Corresponding author at: School of Materials Science and Engineering, Wuhan University of Technology, Wuhan 430070, PR China.
E-mail addresses: wujs@whut.edu.cn (J. Wu), ydingaf@whut.edu.cn (Y. Ding), mlq518@whut.edu.cn (L. Mai).
[1] These authors contributed equally to this work.

https://doi.org/10.1016/j.nanoen.2023.108462
Received 7 February 2023; Received in revised form 30 March 2023; Accepted 18 April 2023
Available online 20 April 2023

carbon hosts including CMK-3 [10], MOF [11], 3D reduced graphene oxide aerogel [12] and elastic aerogel of carbon nanotubes (CNTs) [13–19] have been investigated with remarkable performance, the improvement of cycling performance is limited due to the finite spatial confinement effect of these carbon hosts with micro- or macro- porous structures. In addition, these carbon hosts always lack the effective protection of the soluble Li_2Te_n in ether-based electrolyte, which restricts the cycling performance of Li-Te batteries.

More importantly, unlike a one-step reaction in carbonate electrolyte, a two-step redox reaction happens with complex chain-like or cyclo polytelluride ($Li_2[Te_n]^{2-}$, $2 < n \leq 8$) intermediates in ether-based electrolyte during the cycling [12,20]. Whereas, lots of the reported works only observe one broad plateau during the charge process in experiment. Therefore, the detailed conversion reaction mechanism for Li-Te batteries in ether-based electrolyte, especially the structure changes of Te, is still blurred.

In this work, we prepare a cathode material based on polycrystalline Te encapsulated in N-doped multiwall carbon nanotubes (Te-filled CNTs) by a physical vapor transport (PVT) method and thoroughly investigate the electrochemical reaction mechanism of Li-Te batteries. The cathodes with Te-filled CNTs show a specific capacity of 590 mAh g^{-1} (based on Te mass), which is much higher than the theoretical specific capacity of Te (420 mAh g^{-1}). Taking the advantage of the unique nanoconfinement effect of CNTs, the structural transformation of Te during electrochemical conversion reaction can be clearly detected and observed by a series of *in situ* characterizations. Specially, a clear two-step lithiation/delithiation process is revealed straightforwardly. The enhancement of the cyclability for Li-Te batteries can be explained by the nanocofinement effect of CNTs, which greatly suppress the drastic volume change and stabilize intermediates during cycling. In addition, theoretical calculations based on density functional theory (DFT) further prove that Te in CNTs offers a lower energy barrier for the lithiation. This work fundamentally reveals the conversion reaction mechanism of Li-Te batteries and demonstrates an effective method to boost the electrochemical performance of Li-Te batteries by stabilizing the polytelluride intermediates.

2. Experimental section

2.1. Acid treatment of MWCNTs

To remove the amorphous carbon and introduce defects on the surface, 100 mg pristine MWCNTs (Nanjing XFNANO Materials Tech Co., Ltd.) were first ultra-sonicated in 100 ml HNO_3 (65 %, wt./wt %) at room temperature for 10 min, then refluxed at 100 ℃ for 4 h. Dilute the cooled mixture solution in deionized water (DI water) and wash with a vacuum filter until the pH reaches neutral. After freeze-drying, acid-treated MWCNTs were obtained.

2.2. Synthesis of Te-filled CNTs and bare CNTs

20 mg acid-treated MWCNTs and 200 mg Te (99.999 %, metals basis) power were sealed in ampoule tubes under vacuum (10^{-2} Pa) and heated at 850 °C for 24 h. Then, the as-prepared Te-filled CNTs were heated at 380 °C for 20 min to remove the residual Te. The same materials except Te were used to prepare bare CNTs in the same way of Te-filled CNTs for comparison.

2.3. Preparation of Te nanowires and Te/CNTs

The synthesis of Te nanowires (Te NWs) was based on the previous work [21]. To synthesize Te/CNTs, 60 mg acid-treated MWCNTs and 60 mg Te NWs were added in 100 ml DI water. After ultrasonication and stirring for 2 h, the solution was freeze-dried to obtain Te/CNTs.

2.4. Materials characterization

X-ray diffraction (XRD) was conducted to investigate the sample structure by using a Burker D8 Discover X-ray diffractometer with Cu-Kα radiation. The high-resolution transmission electron microscopy (HRTEM) images, high angular annular dark field scanning transmission electron microscopy (HAADF-STEM) images and *in situ* TEM result were gained by utilizing a Thermo Fisher Talos F200S transmission electron microscope operated at 200 kV. X-ray photoelectron spectroscopy (XPS) analysis was carried out on Escalab 250Xi. Raman characterizations were measured with green laser (532 nm) using LABRAM HR Evolution Raman spectrometer. Thermogravimetric analyzer (TGA) was performed on a Netzsch STA-449 C thermobalance with a temperature ramp of 10 ℃ min^{-1} under an argon gas.

2.5. Electrochemical measurements

Active materials of Te-filled CNTs, Te/CNTs or bare CNTs were mixed with conductive carbon black (Acetylene black) and binder (polyvinylidene fluoride) (8:1:1, weight ratios) in an N-methyl-2-pyrrolidone solvent to form an electrode slurry. Then, the slurry was coated on an aluminum foil to form the working electrode (100 μm). The mass load in this cathode is ~1 mg cm^{-2}. Electrochemical experiments were conducted based on the coin cell (CR2025-type) by using Li metal (15.6 × 0.45 mm) as the anode and Celgard 2500 as the separator. The electrolyte was a solution of 1 M LiTFSI (DME:DOL) (1:1 by volume) with 1 wt % $LiNO_3$ (60 μl). Additionally, cyclic voltammetry (CV) and electrochemical impedance spectroscopy (EIS) were conducted with EC-LAB. All the tests were carried out at room temperature. CV measurements were performed at a scan rate of 0.1 mV s^{-1} in the voltage range from 1.0 to 3.0 V. EIS tests were carried out at open-circuit potential in the frequency range between 100 kHz and 0.01 Hz. Galvanostatic charge/discharge (GCD) measurements were performed in the voltage range of 1.0–3.0 V by the Neware CT-4000 multichannel battery test system.

2.6. In situ measurements

The special battery model was used for these measurements. For the *in situ* Raman spectroscopy, it was collected in Renishaw INVIA micro-Raman spectroscopy system. A 532 nm excitation laser was employed with a cumulative time of 100 s. The *in situ* XRD signals were collected by using the VANTEC-500 detector in a still mode and each diffraction pattern was collected for 120 s. During measurements, the X-rays penetrate the beryllium window on the battery model and detect the signal of structural evolution. Current density of 50 mA g^{-1} was used in both *in situ* measurements. *In situ* TEM were carried out with the *in situ* electric biasing holder (ZepTools Co. Ltd., China) on the Talos F200s.

2.7. DFT calculations

All DFT calculations in this paper are conducted based on the Vienna Ab-inito Simulation Package (VASP) [22,23]. The electron-ion interaction is described by the Projected Augmented-Wave (PAW) potentials, and the exchange-correlation interactions are calculated by the Perdew-Burke-Enzerhof (PBE) pseudopotentials of Generalized Gradient Approximation (GGA) [24,25]. The plane-wave energy cutoff is set as 450 eV. The convergence threshold is set as 1.0×10^{-4} eV in energy and 0.02 eV per Angstrom in force. The Brillouin zone was sampled with 3 × 3 × 3 k-points. A vacuum space of 15 Å is inserted in z direction to avoid interactions between periodic images. The calculation formula of binding energy is as follows:

$$E_{ads} = E_{(A+B)} - E_{(A)} - E_{(B)}$$

where E_{ads} mean the adsorption energy, $E_{(A+B)}$ represents the calculated

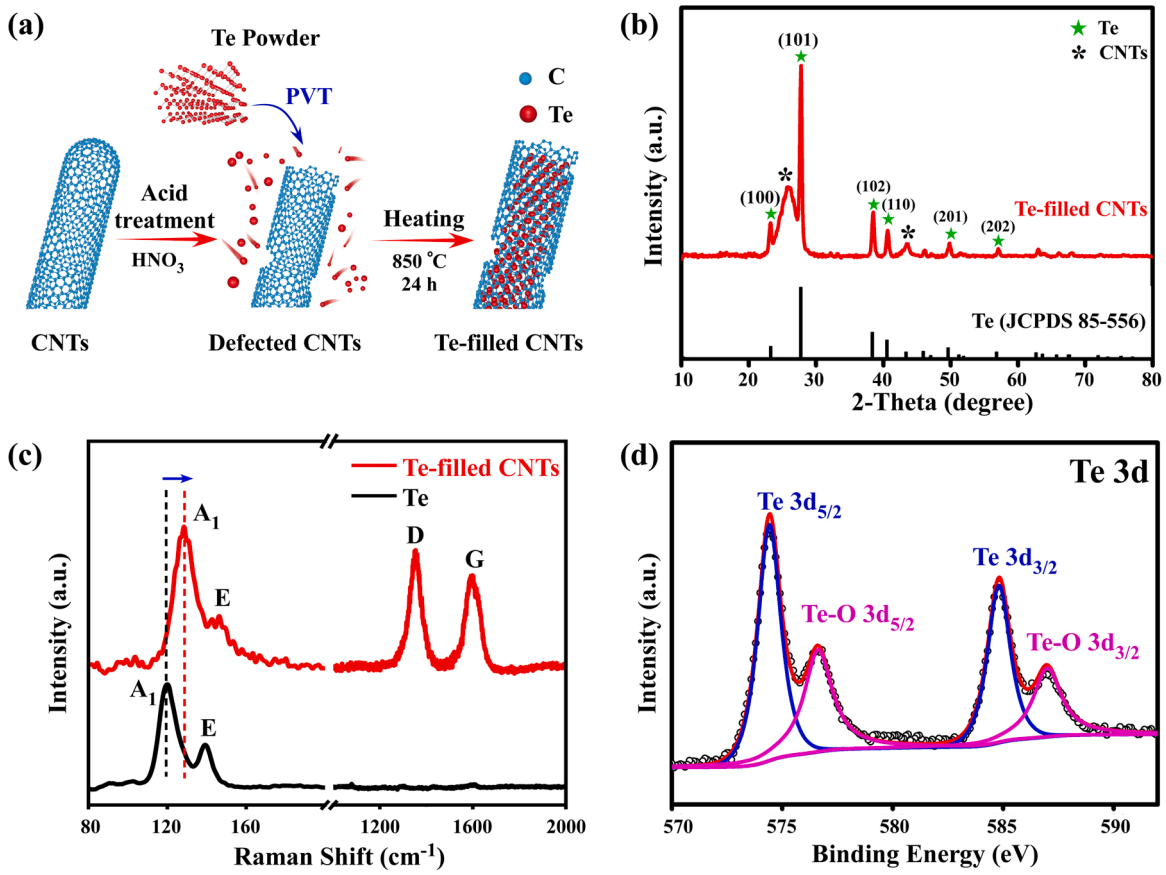

Fig. 1. Synthesis and characterizations of the Te-filled CNTs. (a) Schematic illustration of a typical preparation process of Te-filled CNTs. **(b)** XRD characterization of Te-filled CNTs, compared with standard Te crystals. **(c)** Raman spectra of the Te-filled CNTs and Te nanowires. **(d)** XPS analysis of the Te 3d spectrum for Te-filled CNTs.

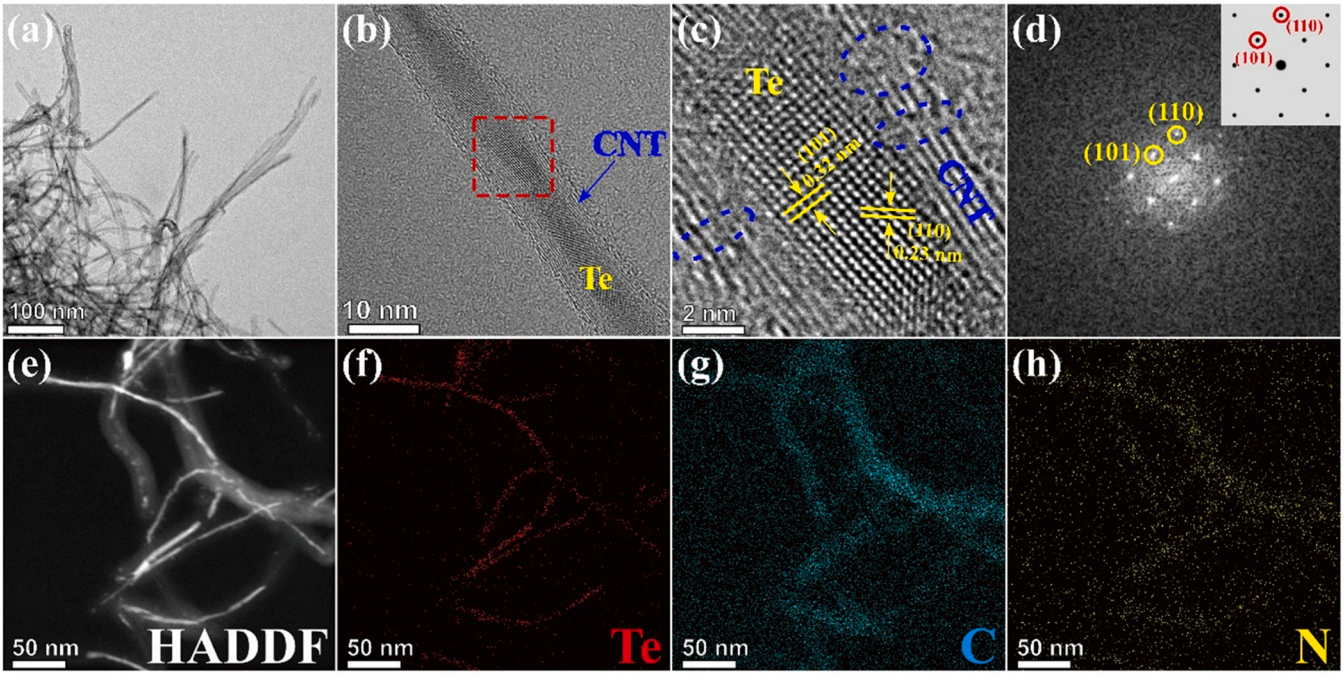

Fig. 2. TEM images of the Te-filled CNTs. (a) Low-magnification and **(b)** high-magnification TEM images of Te-filled CNTs. **(c)** The enlarged image of the red rectangular area in (b), showing Te nanocrystal along the [−111] zone axis where the (101) and (110) lattice planes are marked, and confined in CNT. **(d)** The corresponding FFT pattern of (c). (Inset: the standard diffraction patterns of Te). **(e)** The HADDF image and the corresponding elemental mapping images of **(f)** Te, **(g)** C, and **(h)** N for Te-filled CNTs.

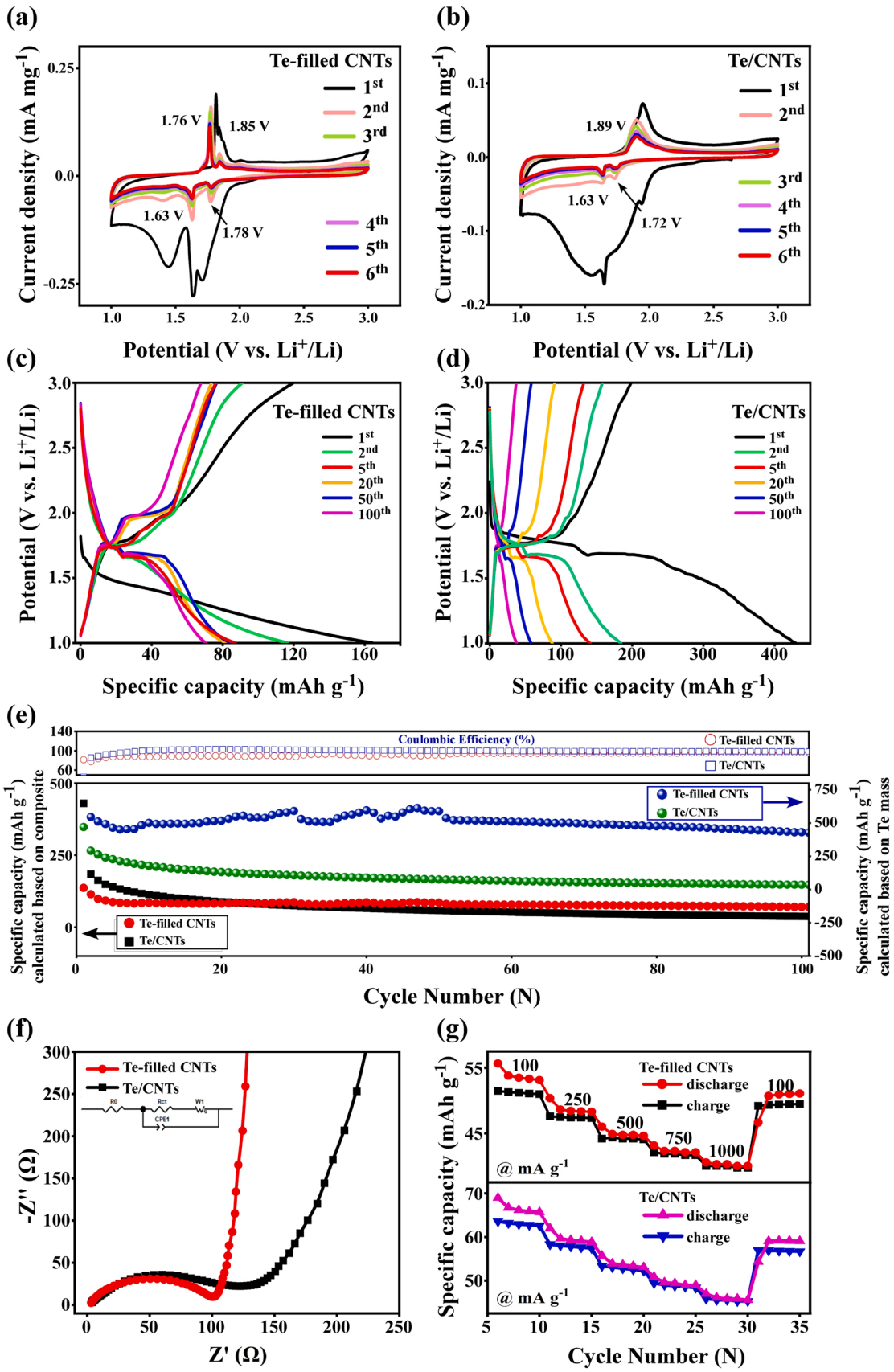

Fig. 3. Electrochemical properties of Te-filled CNTs cathodes for Li-Te batteries. (a) and **(b)** CV curves of Te-filled CNTs and Te/CNTs cathodes at a scan rate of 0.1 mV s^{-1} during the 1st-6th cycles, respectively. **(c)** and **(d)** GCD curves of Te-filled CNTs and Te/CNTs cathodes at a current density of 50 mA g^{-1}, respectively. **(e)** Cyclic performance of Te-filled CNTs and Te/CNTs cathodes discharged at a current density of 50 mA g^{-1} for 100 cycles. **(f)** EIS spectra of the Te-filled CNTs and Te/CNTs fresh cells. **(g)** Discharge/charge performance of Te-filled CNTs and Te/CNTs cathodes at different current density.

energy of adsorption configuration, $E_{(A)}$ and $E_{(B)}$ are the calculated energy of substrate and adsorbent respectively.

3. Results and discussions

The typical synthesis process for Te-filled CNTs is schematically illustrated in Fig. 1**a** (See the **Experimental section** for details). Before Te-filling, CNTs are suspended in concentrated nitric acid and refluxed for 4 h in order to open the ends of CNTs and create defects at the nanotube walls. The acid treatment is critical for the Te-filling, since the opening ends and defects are the entrance for Te atoms during PVT step (Fig. S2). Then, Te powder and CNTs are sealed in the ampoule tube (Fig. S3), which is heated to 850 ℃ for 24 h to obtain the Te-filled CNTs. The mass of Te in Te-filled CNTs is about 8 % (Fig. S1), which is close to the previously reported work of PVT [26,27]. Here, different from the loading method by melted Te, the filling of Te inside the CNTs is achieved *via* the vapor phase transport. Therefore, a much higher heating temperature compared with the melting point of Te is applied to create a high Te vapor pressure to facilitate the filling of Te inside the CNTs [26, 27], as the Te loading is only 3 wt % when the heating temperature is 500 ℃ (Fig. S4).

Fig. 1**b** shows the X-ray diffraction (XRD) patterns of the Te-filled CNTs. The peaks at 26° and 43° can be indexed to CNTs, while the surplus peaks fit perfectly with the standard patterns of triclinic tellurium (JCPDS No. 85–556). It should be noted that no other peaks of impurities can be observed, proving the pure crystallinity of Te in CNTs. Raman spectra of Te-filled CNTs and pure tellurium nanowires (Te NWs) are compared in Fig. 1**c**. Two characteristic peaks located at 120 cm^{-1} (A_1 mode) and 140 cm^{-1} (E mode) can be clearly detected in Te NWs, consistent with previous reports [21,28]. For Te-filled CNTs, these two peaks of Te can also be observed but with a small blue shift to 128 cm^{-1} and 146 cm^{-1}. This is because that when Te is nanoconfined, for which the unique chiral structure of Te can strengthen the inter-chain interactions and weaken the inter-chain interaction of Te and CNTs, resulting in the shift [21]. Moreover, two peaks at 1351 cm^{-1} and 1586 cm^{-1} can be detected in Te-filled CNTs, representing the D band and G band of CNTs, respectively [29]. Notably, the I_D/I_G intensity ratio for Te-filled CNTs (1.31) is higher than that for pristine CNTs (1.06) (Fig. S5), suggesting the formation of defects caused by acid treatment in Te-filled CNTs. Furthermore, to determine the elemental states in Te-filled CNTs, X-ray photoelectron spectroscopy (XPS) analysis of Te 3d is conducted (Fig. 1**d**). The spectrum reveals the Te $3d_{5/2}$ peak at 574.4 eV and the Te $3d_{3/2}$ peak at 584.8 eV, corresponding to the metallic state of Te in CNTs [30]. Meanwhile, peaks at 576.6 eV and 586.9 eV refer to the Te-O bonds formed between Te and oxygen-containing functional groups on acid treated CNTs [31]. Combined with XRD and Raman results **(**Fig. 1 **and** Fig. S6**)**, the TeO_2 in Te-filled CNTs is negligible, which has little effect on the electrochemical performance. Interestingly, the binding energy of Te-Te bonds of Te-filled CNTs was higher than that of the bulk Te [30]. The increased binding energy in Te-filled CNTs indicates a charge-deficient state of Te during its interaction with CNTs that possesses higher electronegativity [17]. Therefore, the stronger Te-C interaction is believed to be beneficial for effective confinement of Te and polytelluride.

To get a clear view of the nanoscale structure of Te-filled CNTs, HRTEM is conducted as shown in Fig. 2. Fig. 2**a** is the low-magnitude TEM image for Te-filled CNTs, in which it can be found that most Te nanocrystals are well encapsulated in cavities of CNTs (4–6 nm) with negligible outside Te (Fig. S7). Besides, plenty of opening ends are observed in CNTs after acid treatment. In comparison, less Te is encapsulated in the CNTs without acid treatment (Fig. S8), which validates the importance of these opening ends for Te filling. Fig. 2**b** is the high-magnitude TEM image of a single tube filled with Te, showing the polycrystalline nature of Te. Fig. 2**c** shows the enlarged TEM image of the red rectangle area in Fig. 2**b**, which presents the high density of defects formed on the walls of CNT. Besides, the distinctive lattice fringes belonging to Te nanocrystals can be clearly observed with the lattice spacing $\boldsymbol{d} = 0.32$ nm and 0.23 nm, corresponding to the (101) and (110) lattice planes of triclinic Te, respectively. The fast Fourier transform (FFT) patterns (Fig. 2**d)** of Fig. 2**c** further demonstrate that the nanoconfined Te in CNTs are highly crystallized matching well with the standard patterns of Te (ICSD NO.023060), consistent with the XRD results. To provide a direct view of the elemental distribution of Te-filled CNTs, the energy dispersive spectroscopy (EDS) elemental mapping images are presented in Fig. 2**e-h** for Te, C and N, respectively. In Fig. 2**h**, it should be noted that the CNTs are doped by N from the reaction with HNO_3, which is beneficial for the improvement of electrical conductivity [32–34]. These effects can further enhance the kinetics of the electrochemical conversion reaction of Te in tubes during the charge/discharge cycles.

Fig. 3 shows the electrochemical performance of Te-filled CNTs as cathodes in Li-Te batteries. The Te/CNTs prepared by physically mixing Te (50 wt %) with CNTs are tested for comparison. The 1st-6th cyclic voltammetry (CV) results of Te-filled CNTs and Te/CNTs at a scanning rate of 0.1 mV s^{-1} in the voltage range of 1.0 V~3.0 V are shown in Fig. 3**a** and 3**b**, respectively. Two cathodic peaks at 1.72 V and 1.63 V are observed in the CV curves of Te/CNTs, which correspond to the formation of lithium polytellurides (Li_2Te_n) and Li_2Te, respectively [12, 35]. In the subsequent anodic scan, there is a broad anodic peak at 1.89 V referring to the reverse process from Li_2Te to Te. For Te-filled CNTs, the cathodic CV curves exhibit two peaks at 1.78 V and 1.63 V as shown in Fig. 3**a**, similar to Te/CNTs. However, unlike that in Te/CNTs, in the subsequent anodic scan, two separate peaks are detected at 1.76 V and 1.85 V, which refer to the formation of Li_2Te_n and Te, respectively. The sharp peak at 1.76 V indicates the fast reaction kinetics of the formation of Li_2Te_n which can be stabilized inside the CNTs during the two-step delithiation. More importantly, the difference between the anodic and cathodic peaks of Te-filled CNTs is significantly smaller than that of Te/CNTs, which suggests that the lithiation/delithiation of Te-filled CNTs is electrochemically more reversible. This phenomenon can be explained by the nanoconfined effect of CNTs which prevents the dissolution of Li_2Te_n in electrolyte and provides a directional transportation channel for Li^+ during the cycles. The above mechanism will be extensively explored by *in situ* Raman and XRD characterizations. Galvanostatic charge/discharge (GCD) profiles for two samples are presented in Fig. 3**c** and 3**d**. In Fig. 3**c**, Te-filled CNTs cathodes show two discharge plateaus at ~1.74 V and ~1.66 V along with two charge plateaus at ~1.76 V and ~1.92 V, consistent with the CV results in Fig. 3**a**. In comparison, Te/CNTs composites exhibit initially two discharge plateaus and one charge plateau, and a fast capacity decay over cycles. The prominent charge plateau at ~1.92 V for Te-filled CNTs implies that the Li_2Te_n formed in the first delithiation step is preserved inside the CNTs, which undergoes a reversible conversion and deconversion process in the following cycles. As a result, the cycling performance of Te-filled CNTs is greatly enhanced. In addition, the IR drops shown in Te-filled CNTs are caused by the relatively high discharge rate of 50 mA g^{-1} for the low Te loading (8 wt %) cathodes, which can also be observed in previous reports [12,13].

The cycling performance of Te-filled CNTs cathodes is shown in Fig. 3**e**. The current density applied in this work is determined by the total mass of the composite, which is very common for electrode materials based on nanoconfined materials in CNTs [26,36–39]. It should be noted that both Te-filled CNTs and Te/CNTs show a relatively low coulombic efficiency during the initial cycles (Fig. S9), which is common for most carbon based hosts cathodes [14,40]. The irreversible capacity loss is mainly due to the irreversible reaction of Li^+ with functional groups (*e.g.*, -OH and -COOH) on CNTs introduced by acid treatment, and the formation of SEI layers, which result from decomposition of electrolyte during initial cycles [41,42]. Here, the lower coulombic efficiency of Te-filled CNTs is due to the higher content of CNTs (> 90 %) compared with Te/CNTs (50 %). In addition, the coulombic efficiency of the bare CNTs during cycling is illustrated in Fig. S10 which is the lowest

Table 1
Comparison of the performance of this work and references in Li-Te batteries.

Cathode	Electrolyte	Specific Capacity (after stabilized)	Cycling Performance	Capacity loss per cycle	Voltage Range
This work	**1 M LiTFSI in DOL:DME with 1 % $LiNO_3$**	**465.5 mAh g^{-1} at 50 mA g^{-1}**	**430.6 mAh g^{-1} after 100 cycles at 50 mA g^{-1}**	**0.075 %**	**1.0–3.0 V**
Te/MPC [6]	1 M LiTFSI in DOL:DME	322 mAh g^{-1} at 1 C	274 mAh g^{-1} after 1000 cycles at 1 C	0.015 %	1.0–2.7 V
Te/C [5]	1 M $LiPF_6$ in EC:DEC	317 mAh g^{-1} at 50 mA g^{-1}	241 mAh g^{-1} after 200 cycles at 50 mA g^{-1}[a]	0.12 %	0.8–2.5 V
Te/CMK-3 [10]	1 M $LiPF_6$ in EC:DEC	286 mAh g^{-1} at 10 C	243.1 mAh g^{-1} after 990 cycle at 10 C	0.015 %	1.0–3.0 V
Te@C-Co-N [11]	1 M LiTFSI in DOL:DME	398.1 mAh g^{-1} at 1 C	372 mAh g^{-1} after 800 cycles at 1 C	0.008 %	1.0–3.0 V
Te/3DGO [12]	1 M LiTFSI in DOL:DME	391.5 mAh g^{-1} at 1 C	270 mAh g^{-1} after 500 cycles at 1 C	0.062 %	1.0–3.0 V
Te@CNT aerogel (porous structure) [13]	1 M LiTFSI in DMSO	400 mAh g^{-1} at 0.1 C	326 mAh g^{-1} after 100 cycles at 0.1 C	0.18 %	1.0–2.7 V
NPCS/Te [16]	1 M LiTFSI in DOL:DME	420 mAh g^{-1} at 0.25 C[a]	310 mAh g^{-1} after 200 cycles at 0.25 C	0.13 %	1.0–3.0 V
MR-Te/C [19]	1 M $LiPF_6$ in EC:DEC	329 mAh g^{-1} at 100 mA g^{-1}	252 mAh g^{-1} after 100 at 100 mA g^{-1}	0.5 %	1.0–3.0 V

[a] Estimated value based on the cycling performance data.

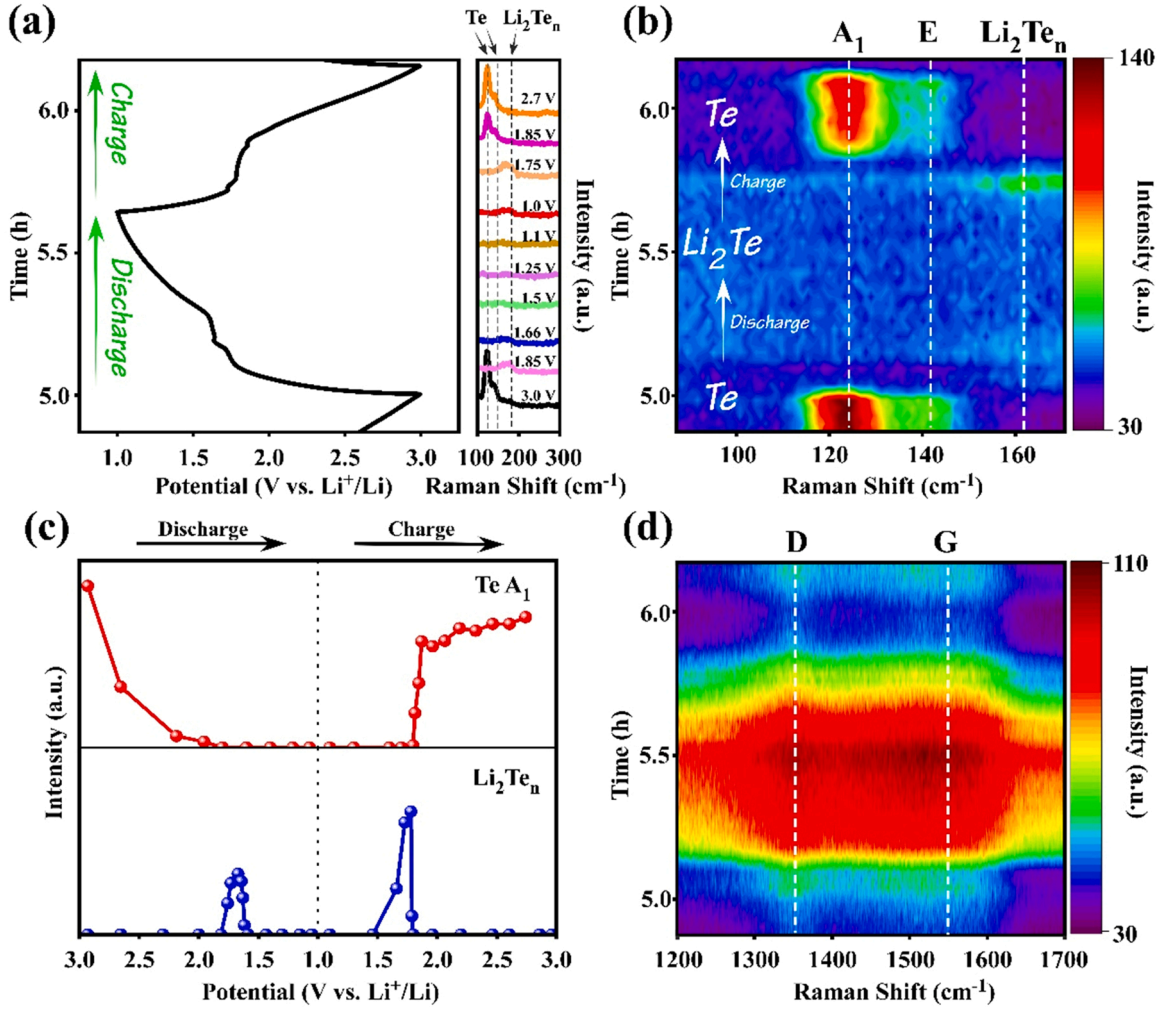

Fig. 4. ***In situ*** **Raman characterization of Te-filled CNTs during the charge/discharge process. (a)** GCD curves of the second cycle during *in situ* Raman measurement, right panel is the *in situ* Raman spectra at different potential. **(b)** and **(d)** Contour plot of Raman spectra for Te-filled CNTs, corresponding to (a). **(c)** Trend diagram of peak intensity of Te (A_1) and Li_2Te_n as a function of potential.

compared with the two composites. The capacity loss of the initial 5 cycles due to the irreversible capacity of CNTs and residual Te particles outside CNTs is observed in CV and cycling performance. The specific capacity with respect to the mass of Te is calculated by subtracting the capacity of bare CNTs (Fig. S11), and the calculation method is based on the previously reported works about active materials confined in CNTs [36]. From the 5th cycle, Te-filled CNTs cathode exhibit a stable cyclic performance at 50 mA g^{-1} with a high specific capacity of 87.2 mAh g^{-1} (465.5 mAh g^{-1} based on Te mass) and a final specific capacity of 70.4 mAh g^{-1} (430.6 mAh g^{-1} based on Te mass) after 100 cycles.

Distinctively, the specific capacity of Te gradually enhanced during cycles reaching a maximum of 590 mAh g^{-1} at the 50th cycle, due to the

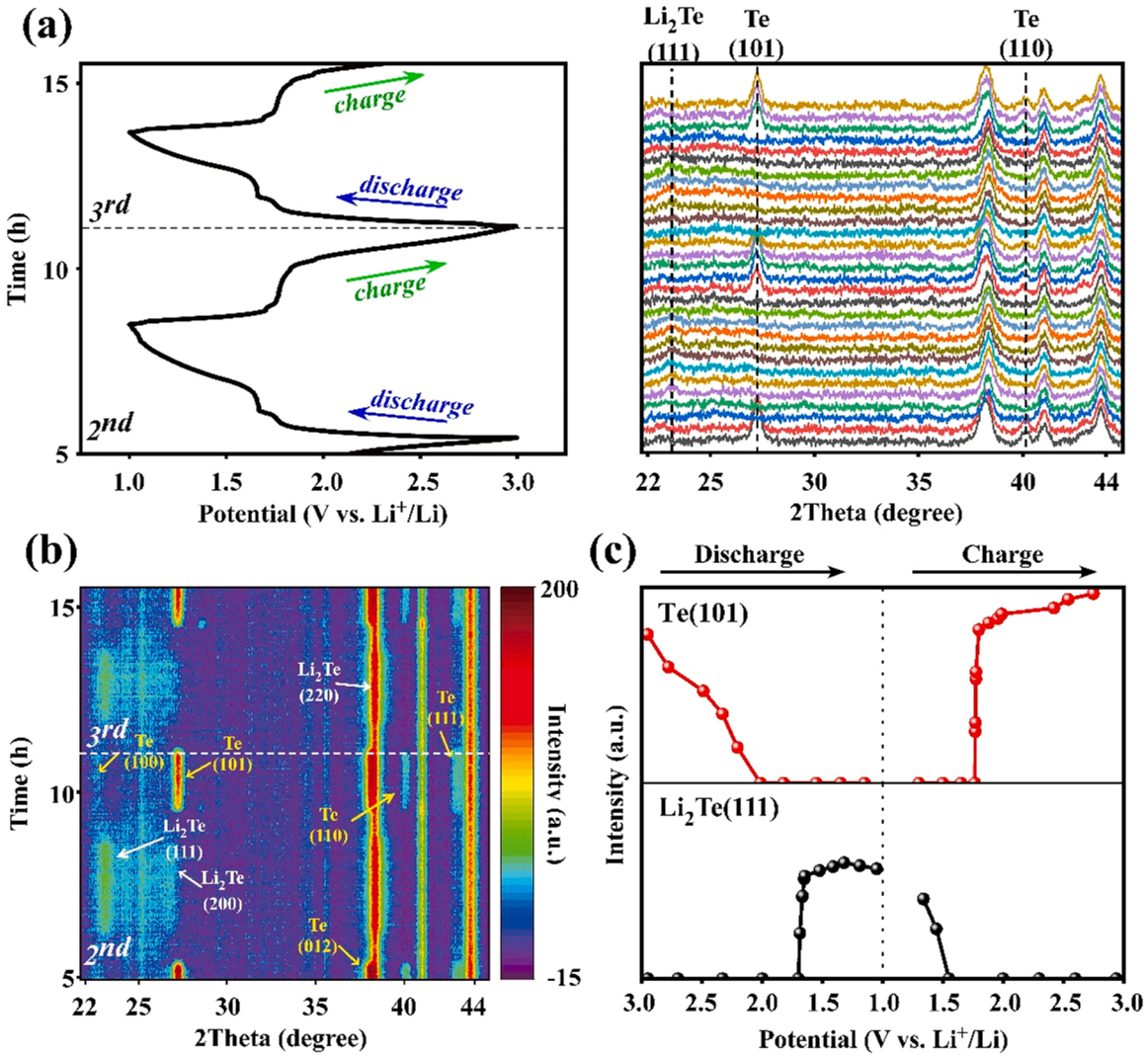

Fig. 5. ***In situ*** **XRD characterization of the 2nd to 3rd charge/discharge cycles. (a)** GCD curves of the second and third cycle during *in situ* XRD measurements (50 mA g^{-1}), right panel is the *in situ* XRD patterns. **(b)** Contour plot of the *in situ* XRD patterns from (a), which indicates the intensity changes of the characteristic peaks of Te and Li_2Te during the cycles. **(c)** Trend diagram of peak intensity of Te (101) and Li_2Te (111) as a function of potential.

activation process with full infiltration by the electrolyte and the reversible formation of polymeric gel-like layers arising from electrolyte degradation [38,43]. These effects conduce to a specific capacity exceeded the theoretical specific capacity of Te (420 mAh g^{-1}). Similar phenomenon has also been reported in previous works about other CNTs confined electrodes [36,38]. Moreover, the defects of the CNTs greatly affects the electrochemical performance of the cathodes. As the duration of acid treatment increases (*e.g.*, 8 h), more defects can be identified (Fig. S12). Since more defects on CNTs can facilitate the filling of Te during the PVT process, the initial specific capacity of 8 h sample is higher than that of 4 h. However, too many pores will cause serious damage to the stability of cathodes, and will inhibit the protection of the dissolution of Li_2Te_n (Fig. S13). The cycling stability of our work is among the best of reports in Li-Te batteries based on carbon hosts as listed in Table 1.

The electrochemical impedance spectroscopy (EIS) in Fig. 3**f** further proves the above conclusions. The straight-line slope of Te-filled CNTs is significantly higher than that of Te/CNTs in the high frequency zone, indicating a faster diffusion speed for Li^+ in Te-filled CNTs. Besides, the rate performance of two cathodes is also compared with the increase of current density from 100 mA g^{-1} to 1000 mA g^{-1}. The separate specific capacity of Te for the rate performance is shown in Fig. S14. The Te-filled CNTs cathode can deliver a reversible discharge specific capacity (based on Te mass) of 438.4, 404.6, 378.9, 358.3 and 342.1 mAh g^{-1} at 100, 250, 500, 750 and 1000 mA g^{-1}, respectively. In the Te-filled CNTs cathode, the specific capacity can be well recovered (419.1 mAh g^{-1}) as the current density recovered to 100 mA g^{-1}, which demonstrates a good rate performance.

To further reveal the structural evolution and redox chemistry of Te-filled CNTs during lithiation/delithiation, *in situ* Raman and XRD characterizations are employed. Fig. 4**a** presents the GCD curves of Te-filled CNTs in the second cycle which is conducted in the voltage between 1.0 and 3.0 V at a current density of 50 mA g^{-1}. In the meantime, *in situ* Raman characterization is conducted continuously with a few of typical results at different time plotted in the right panel of Fig. 4**a**. The corresponding contour plot is illustrated in Fig. 4**b** and 4**c** (Fig. S15 for *in situ* Raman results in more long-term charge/discharge cycles). In the discharge process, along with the Li^+ insertion, the intensity of A_1 mode (128 cm^{-1}) and E mode (146 cm^{-1}) of Te encapsulated by CNTs is gradually weakened (Fig. 4**a** right panel), consistent with the conversion reaction from Te to long-chain Li_2Te_n before 2.0 V. This is in combination with the peak at 169 cm^{-1} appearing at 1.78 V, known as the formation of chainlike or cyclo-Li_2Te_n [11]. To describe the change of Te and Li_2Te_n peaks more precisely, the intensity of Te (A_1) and Li_2Te_n is further plotted as the change of potential in Fig. 4**c**. It can be observed that intensity of Te (A_1) mode declines from ~2.7 V and vanishes at

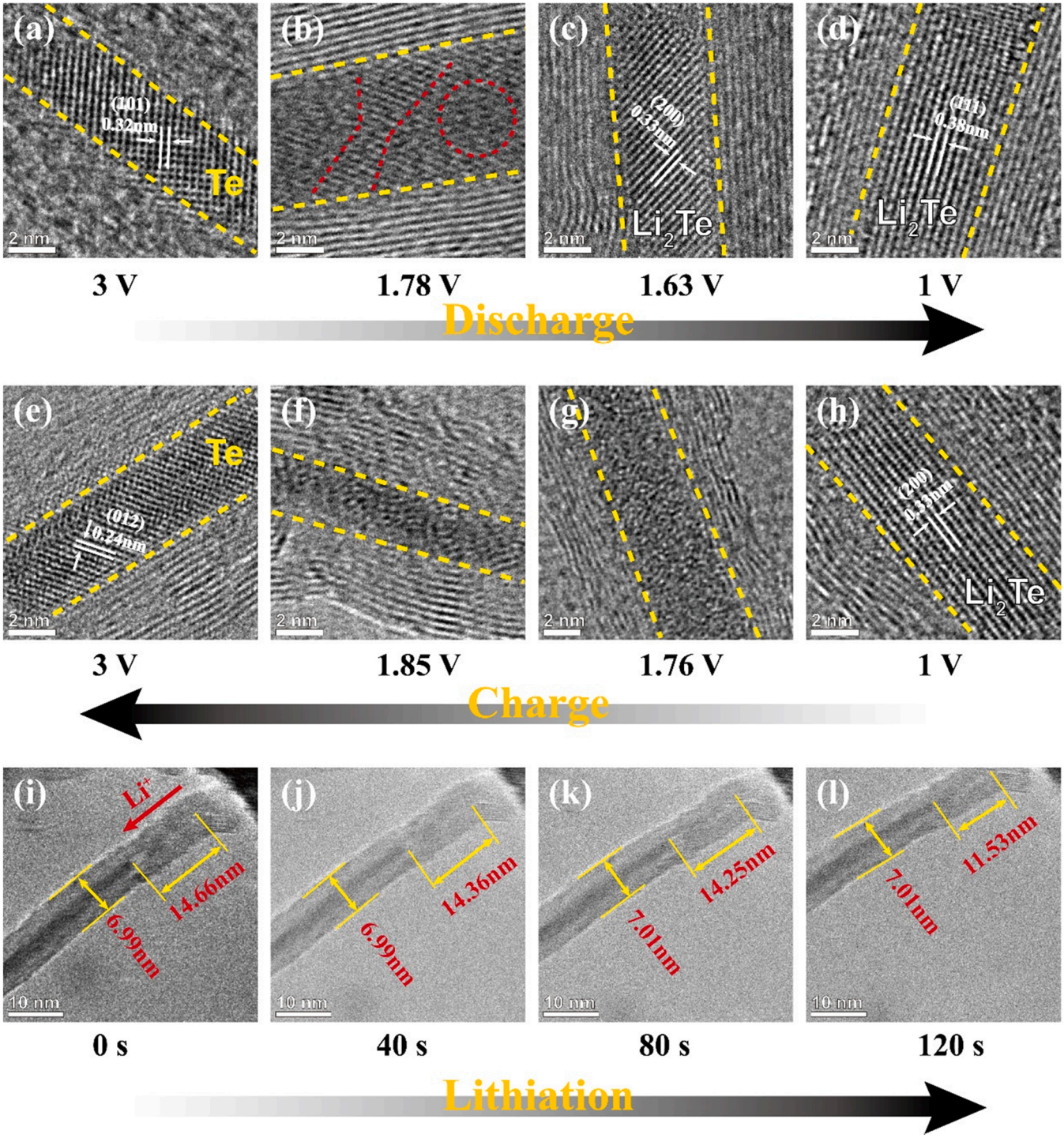

Fig. 6. ***Ex situ*** **and** ***in situ*** **TEM characterization of a single nanotube. (a)-(h)** Structural evolution of Te filled in CNTs during discharge (a-d) and charge process (e-h) by *ex situ* HRTEM. **(i)-(l)** Snapshots of Te-filled in CNT during lithiation by *in situ* TEM.

~2.0 V in the discharge, which appears again at ~1.85 V and increase continuously till 3 V in the charge. For Li_2Te_n, the peak shows up from 1.78 V to 1.68 V voltage range in the both discharge and charge step.

Besides, it is worth mentioning that D and G bands of CNTs also change during charge/discharge process. As shown in Fig. 4**d**, during the discharge process, the intensity of peaks located at 1351 cm^{-1} (D band) and 1586 cm^{-1} (G band) are greatly enhanced and broadened at ~1.75 V, both D and G band reach the highest peak intensity at the end of cathodic reaction. On the other side, during the charge process, the intensity of two peaks decreases dramatically from beginning to ~1.8 V and reaches the lowest at the end of anodic reaction. This phenomenon can be explained by the change of plasmon-phonon and phonon-phonon interactions between CNT and the filling atoms due to the electrochemical reaction in the charge/discharge process, which indicates a strong interaction between the filling Te atoms and CNTs [44]. In contrast, there are no such changes in bare CNTs cathodes without Te (Fig. S16). Thus, during the charge/discharge process, CNTs in Te-filled CNTs cathodes prevent structure pulverization and dissolution of the electrodes, which synergisticly enhance the long cyclic performance.

To further investigate the evolution of Li_2Te during electrochemical

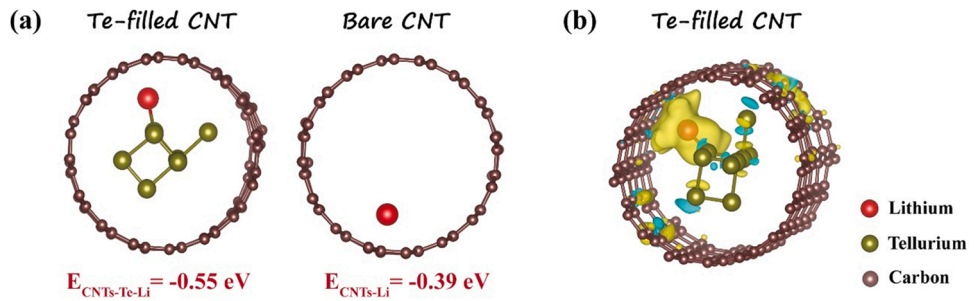

Fig. 7. DFT calculations to illustrate the high capacity and long cyclic stability of the Te-filled CNTs. (a) DFT calculations for the formation energy of Li^+ on Te filled in CNTs (left image) and the concave surface of bare CNTs (right image). **(b)** Charge density differences on Te-filled CNTs at the beginning of lithiation. The yellow and blue area represent the regions of charge gain and lost, respectively.

reaction, *in situ* XRD is performed. Fig. 5**a** depicts the evolution of XRD patterns of the Te-filled CNTs cathodes during the second and third cycles between 1.0 and 3.0 V at a constant current rate of 50 mA g^{-1}. Before the test, an *ex situ* XRD is conducted to characterize the electrodes before and after cycles (Fig. S17). From the *ex situ* XRD, most of the final products of Te-filled CNTs cathodes after discharge are Li_2Te, which is consistent with the TEM results in Fig. 6. As shown by the contour plot in Fig. 5**b**, the peak intensity of Te decreases rapidly with lithiation and then disappears at ~2.2 V, corresponding to the transformation for Te into long-chain Li_2Te_n. When discharged at ~1.64 V, the three diffraction peaks of the final products as Li_2Te (111), (200) and (220) appear at 23.1°, 26.8° and 38.4°, respectively. Here, the peak around 38.3° is overlapped by multiple diffraction peaks, which contains Te (012), Li_2Te (220) and BeO (100). With the lithiation of Te, this broad peak shifts to the right and shifts back after delithiation. Meanwhile, during the charge process, the intensity of peaks for Li_2Te are significantly weakened. However, the diffraction peaks of the intermediates (Li_2Te_n) are not clearly observed during the two charge/discharge cycles, which is due to the low crystallinity of the intermediate phase. Nevertheless, the formation of such intermediate phase can be identified by *in-situ* TEM investigation (Fig. 6), which has advantage in characterizing the phase structure of nano-scale crystals [45]. To quantitatively clarify the reaction process during the cycling, the intensity changes of Te (101) and Li_2Te (111) peaks in the 2nd cycle is plotted in Fig. 5**c**. In the discharge process, the intensity of Te (101) decreases as the lithiation proceeds and disappears at 2.11 V, while the Li_2Te (111) peak does not appear until it drops to 1.64 V. Therefore, the lithiation product in the voltage range from 2.11 V to 1.64 V should be Li_2Te_n. Similarly, in the charge process, the Li_2Te (111) peak intensity decreases continuously to zero at 1.45 V along with the appearance of a sharp increase of Te (101) peak at around 1.8 V. Notably, the steep slope of the intensity curves at the edges indicates a thermodynamically equilibrium phase change process during the lithiation/delithiation reaction, which matches well with the prominent plateaus in the galvanostatic curves.

Therefore, in combination with *in situ* Raman results discussed above, the two-step lithiation/delithiation mechanism of Te-filled CNTs cathode can be described as follows:

In discharge:

$$\text{First Step}_{(2.7\ \text{V}—1.76\ \text{V})}: (n/8)Te_8 + 2e^- + 2Li^+ \rightarrow Li_2Te_n \quad (2 < n \leq 8).$$

$$\textit{Second Step}_{(1.76\ \text{V}—1.64\ \text{V})}: Li_2Te_n + (2n-2)e^- + (2n-2)Li^+ \rightarrow nLi_2Te.$$

In charge:

$$\text{First Step}_{(1.0\ \text{V}—1.8\ \text{V})}: nLi_2Te - (2n-2)e^- \rightarrow Li_2Te_n + (2n-2)Li^+.$$

$$\textit{Second Step}_{(1.8\ \text{V}—2.0\ \text{V})}: Li_2Te_n - 2e^- \rightarrow (n/8)Te_8 + 2Li^+ (2 < n \leq 8).$$

Intuitively, to observe the real-time conversion reaction in Te-filled CNTs cathode under the battery operating environment, *ex situ* and *in situ* TEM characterization is conducted during the charge/discharge process as shown in Fig. 6. Taking the advantages of robust structural stability and high electrical conductivity of CNTs, it is feasible to directly observe the real-time changes of the nanoconfined Te during cycles. Fig. 6**a**-6**h** present *ex situ* TEM images of Te inside CNTs at different charge/discharge potentials, from which a transformation between Te and Li_2Te can be clearly observed. Specifically, in Fig. 6**b**, it can be directly observed that the amorphous Li_2Te_n (red circle) forms within the Te crystal, corresponding to the conversion reaction of Te to Li_2Te_n at 1.78 V. Fig. 6**f and** 6**g** give a direct view of the intermediate products, Li_2Te_n with amorphous morphology at 1.85 V and 1.76 V, which is hard to be detected by XRD. Furthermore, *in situ* TEM of a single tube during lithiation process is performed to observe the real-time structural evolution of Te. During *in situ* TEM process, Li^+ migrated along the axial direction of CNT due to a positive bias voltage applied, as shown in Fig. 6**i**. In order to exam the volume expansion of Te in the CNT during lithiation, the diameter of the tube and the distance between Te tip and CNT are carefully measured. From Fig. 6**i**-6**j**, it can be seen that the length of Te gradually increases as Li^+ immigrating from outside to inside of the tube, showing an obvious shorten of the distance between Te tip and CNT (14.66–11.53 nm). On the contrary, the diameter of CNT stays almost the same before and after lithiation. Therefore, the above TEM results prove that the CNT host is able to guide the volume change of Te in axial direction and retain the compact structure of Te/Li_2Te during cycling, which is beneficial for the long cyclic stability of the Li-Te batteries.

Computations based on DFT are conducted on Te-filled CNTs as well to further explain electrochemical mechanism. Fig. 7**a** shows the comparison of the formation energy for Li^+ in Te-filled CNT and bare CNTs. A smaller formation energy of Li^+ inside Te-filled CNT indicates that Li^+ is inclined to be bonded with Te filled in CNT rather than the bare CNTs. Fig. 7**b** shows the charge density difference analysis of Te-filled CNTs at initial lithiation. The yellow and light-blue regions represent electron accumulation and depletion, respectively. It can be clearly seen that when Li^+ is bonded with Te-filled CNT, electrons will accumulate on the concave surface of CNT and the electronegativity gradually increases. While for bare CNT, the curvature of walls will cause the electrons to transfer from the concave to the convex surface of CNTs, which results in a more positive electric potential of the concave surface [46]. During lithiation, excess lithium ions have to be temporally stored in interface to maintain the potential difference between interior surface and exterior surface of CNT [36], which results in an excess lithium storage and a fast Li^+ diffusion kinetic during reaction, consistent with the above electrochemical results.

4. Conclusions

In summary, we have successfully encapsulated polycrystalline Te in CNTs *via* a facile PVT method. When assembled as the cathodes of Li-Te batteries, Te-filled CNTs show high electrical conductivity, structural stability, fast Li^+ diffusion kinetics and polytelluride preservation, which makes the cathodes obtain ultra-high specific capacity and excellent cyclability. Specifically, when compared with Te/CNTs cathodes, the Te-filled CNTs cathodes display a higher specific capacity (590 mAh g^{-1} at 50 mA g^{-1}), a more stable two-step reaction plateaus and

better electrochemical reversibility. A variety of *in situ* and *ex situ* characterizations reveal the two-step reaction discharge/charge mechanism of the Te-filled CNTs cathodes in which the CNT host is able to reduce the capacity loss by reducing the volume change and the polytelluride dissolution during cycling. This work provides a feasible and scalable synthesis approach of Te-based cathodes for high-performance Li-Te batteries, and systematically discloses the electrochemical reaction mechanism of Te in this new type of batteries.

CRediT authorship contribution statement

Shaoqing Rao: Methodology, Investigation, Writing – original draft, Writing – review & editing. **Ruizhe Wu:** Methodology, Supervision, Validation, Writing – review & editing. **Zhu Zhu:** helped with the *in situ* TEM characterization and discussion. **Jinsong Wu:** Resources, Supervision, Validation, Writing – review & editing. **Yao Ding:** Supervision, Validation, Writing – review & editing, Funding acquisition. **Liqiang Mai:** Resources, Supervision, Validation, Writing – review & editing, Funding acquisition.

Declaration of Competing Interest

The authors declare that they have no known competing financial interests or personal relationships that could have appeared to influence the work reported in this paper.

Data availability

Data will be made available on request.

Acknowledgements

We sincerely thank Dr. Tianyou Zhai and Ph.D. candidate Zongdong Sun from Huazhong University of Science and Technology for their kind discussions in this work. This work was supported by the National Key Research and Development Program of China (2020YFA0715000), the National Natural Science Foundation of China (52127816, 61905183 and 52072282) and the State Key Laboratory of Advanced Technology for Materials Synthesis and Processing (WUT: 2022-KF-4).

Appendix A. Supporting information

Supplementary data associated with this article can be found in the online version at doi:10.1016/j.nanoen.2023.108462.

References

[1] C.S. Cheng, S.H. Chung, Rational design of high-performance nickel-sulfur nanocomposites by the electroless plating method for electrochemical lithium-sulfur battery cathodes, Batter. Supercaps 5 (2022), e202100323, https://doi.org/10.1002/batt.202100323.
[2] Y.-C. Huang, H.-I. Hsiang, S.-H. Chung, Investigation and design of high-loading sulfur cathodes with a high-performance polysulfide adsorbent for electrochemically stable lithium–sulfur batteries, ACS Sustain. Chem. Eng. 10 (2022) 9254–9264, https://doi.org/10.1021/acssuschemeng.2c02332.
[3] X. Gao, X. Yang, S. Wang, Q. Sun, C. Zhao, X. Li, J. Liang, M. Zheng, Y. Zhao, J. Wang, M. Li, R. Li, T.-K. Sham, X. Sun, A 3d-printed ultra-high Se loading cathode for high energy density quasi-solid-state Li–Se batteries, J. Mater. Chem. A 8 (2020) 278–286, https://doi.org/10.1039/c9ta10623e.
[4] Y. Cui, X. Zhou, W. Guo, Y. Liu, T. Li, Y. Fu, L. Zhu, Selenium nanocomposite cathode with long cycle life for rechargeable Li-Se batteries, Batter. Supercaps 2 (2019) 784–791, https://doi.org/10.1002/batt.201900050.
[5] Y. Liu, J. Wang, Y. Xu, Y. Zhu, D. Bigio, C. Wang, Lithium–tellurium batteries based on tellurium/porous carbon composite, J. Mater. Chem. A 2 (2014) 12201–12207, https://doi.org/10.1039/c4ta02075h.
[6] J. Zhang, Y.X. Yin, Y. You, Y. Yan, Y.G. Guo, A high-capacity tellurium@carbon anode material for lithium-ion batteries, Energy Technol. 2 (2014) 757–762, https://doi.org/10.1002/ente.201402069.
[7] Z. Chen, Y. Zhao, F. Mo, Z. Huang, X. Li, D. Wang, G. Liang, Q. Yang, A. Chen, Q. Li, L. Ma, Y. Guo, C. Zhi, Metal-tellurium batteries: A rising energy storage system, Small Struct. 1 (2020), 2000005, https://doi.org/10.1002/sstr.202000005.
[8] Y. Zhang, D. Manaig, D.J. Freschi, J. Liu, Materials design and fundamental understanding of tellurium-based electrochemistry for rechargeable batteries, Energy Storage Mater. 40 (2021) 166–188, https://doi.org/10.1016/j.ensm.2021.05.011.
[9] B. Pruthvija, K.P. Lakshmi, U. Harshitha, A comprehensive overview of metal chalcogenides for rechargeable batteries, Mater. Today.: Proc. 71 (2022) 317–324, https://doi.org/10.1016/j.matpr.2022.09.220.
[10] T. Koketsu, B. Paul, C. Wu, R. Kraehnert, Y. Huang, P. Strasser, A lithium–tellurium rechargeable battery with exceptional cycling stability, J. Appl. Electrochem. 46 (2016) 627–633, https://doi.org/10.1007/s10800-016-0959-8.
[11] J. He, W. Lv, Y. Chen, K. Wen, C. Xu, W. Zhang, Y. Li, W. Qin, W. He, Tellurium-impregnated porous cobalt-doped carbon polyhedra as superior cathodes for lithium-tellurium batteries, ACS Nano 11 (2017) 8144–8152, https://doi.org/10.1021/acsnano.7b03057.
[12] J. He, Y. Chen, W. Lv, K. Wen, Z. Wang, W. Zhang, Y. Li, W. Qin, W. He, Three-dimensional hierarchical reduced graphene oxide/tellurium nanowires: a high-performance freestanding cathode for li-te batteries, ACS Nano 10 (2016) 8837–8842, https://doi.org/10.1021/acsnano.6b04622.
[13] J. Xu, S. Xin, J.W. Liu, J.L. Wang, Y. Lei, S.H. Yu, Elastic carbon nanotube aerogel meets tellurium nanowires: a binder- and collector-free electrode for Li-Te batteries, Adv. Funct. Mater. 26 (2016) 3580–3588, https://doi.org/10.1002/adfm.201600640.
[14] N. Ding, S.F. Chen, D.S. Geng, S.W. Chien, T. An, T.S.A. Hor, Z.L. Liu, S.H. Yu, Y. Zong, Tellurium@ordered macroporous carbon composite and free-standing tellurium nanowire mat as cathode materials for rechargeable lithium-tellurium batteries, Adv. Energy Mater. 5 (2015), 1401999, https://doi.org/10.1002/aenm.201401999.
[15] Y. Li, M.-Q. Wang, Y. Chen, L. Hu, T. Liu, S. Bao, M. Xu, Muscle-like electrode design for Li-Te batteries, Energy Storage Mater. 10 (2018) 10–15, https://doi.org/10.1016/j.ensm.2017.07.017.
[16] Y. Li, Y. Zhang, Q. Xu, L. Hu, B. Shen, H. Liu, C. Dai, S. Bao, M. Xu, Nitrogen-doped carbon as a host for tellurium for high-rate Li-Te and Na-Te batteries, ChemSusChem 12 (2019) 1196–1202, https://doi.org/10.1002/cssc.201802598.
[17] Y. Zhang, W. Lu, P. Zhao, M.H. Aboonasr Shiraz, D. Manaig, D.J. Freschi, Y. Liu, J. Liu, A durable lithium–tellurium battery: effects of carbon pore structure and tellurium content, Carbon 173 (2021) 11–21, https://doi.org/10.1016/j.carbon.2020.10.085.
[18] Y. Li, L.Y. Hu, B.L. Shen, C.L. Dai, Q.J. Xu, D.Y. Liu, J. Jiang, Y. Li, M.W. Xu, Rib-like hierarchical porous carbon as reservoir for long-life and high-rate Li-Te batteries, Electrochim. Acta 250 (2017) 10–15, https://doi.org/10.1016/j.electacta.2017.07.124.
[19] J.U. Seo, G.K. Seong, C.M. Park, Te/C nanocomposites for Li-Te secondary batteries, Sci. Rep. 5 (2015) 7969, https://doi.org/10.1038/srep07969.
[20] L. Ma, J. Wu, Y. Li, Y. Lv, B. Li, Z. Jin, Rational design of carbon nanotube architectures for lithium–chalcogen batteries: advances and perspectives, Energy Storage Mater. 42 (2021) 723–752, https://doi.org/10.1016/j.ensm.2021.08.023.
[21] J.K. Qin, P.Y. Liao, M.W. Si, S.Y. Gao, G. Qiu, J. Jian, Q.X. Wang, S.Q. Zhang, S. Y. Huang, A. Charnas, Y.X. Wang, M.J. Kim, W.Z. Wu, X.F. Xu, H.Y. Wang, L. Yang, Y.K. Yap, P.D.D. Ye, Raman response and transport properties of tellurium atomic chains encapsulated in nanotubes, Nat. Electron. 3 (2020) 141–147, https://doi.org/10.1038/s41928-020-0365-4.
[22] G. Kresse, J. Furthmüller, Efficiency of ab-initio total energy calculations for metals and semiconductors using a plane-wave basis set, Comput. Mater. Sci. 6 (1996) 15–50, https://doi.org/10.1016/0927-0256(96)00008-0.
[23] G. Kresse, J. Furthmuller, Efficient iterative schemes for ab initio total-energy calculations using a plane-wave basis set, Phys. Rev. B: Condens. Matter Mater. Phys. 54 (1996) 11169–11186, https://doi.org/10.1103/physrevb.54.11169.
[24] J.P. Perdew, K. Burke, M. Ernzerhof, Generalized gradient approximation made simple, Phys. Rev. Lett. 78 (1997), https://doi.org/10.1103/PhysRevLett.78.1396.
[25] P.E. Blochl, Projector augmented-wave method, Phys. Rev. B: Condens. Matter Mater. Phys. 50 (1994) 17953–17979, https://doi.org/10.1103/physrevb.50.17953.
[26] C. Fu, M.B. Oviedo, Y. Zhu, A. von Wald Cresce, K. Xu, G. Li, M.E. Itkis, R. C. Haddon, M. Chi, Y. Han, B.M. Wong, J. Guo, Confined lithium-sulfur reactions in narrow-diameter carbon nanotubes reveal enhanced electrochemical reactivity, ACS Nano 12 (2018) 9775–9784, https://doi.org/10.1021/acsnano.7b08778.
[27] G. Li, C. Fu, M.B. Oviedo, M. Chen, X. Tian, E. Bekyarova, M.E. Itkis, B.M. Wong, J. Guo, R.C. Haddon, Giant raman response to the encapsulation of sulfur in narrow diameter single-walled carbon nanotubes, J. Am. Chem. Soc. 138 (2016) 40–43, https://doi.org/10.1021/jacs.5b10598.
[28] Y. Du, G. Qiu, Y. Wang, M. Si, X. Xu, W. Wu, P.D. Ye, One-dimensional van der waals material tellurium: Raman spectroscopy under strain and magneto-transport, Nano Lett. 17 (2017) 3965–3973, https://doi.org/10.1021/acs.nanolett.7b01717.
[29] M.S. Dresselhaus, P.C. Eklund, Phonons in carbon nanotubes, Adv. Phys. 49 (2000) 705–814, https://doi.org/10.1080/000187300413184.
[30] Z. Shi, R. Cao, K. Khan, A.K. Tareen, X. Liu, W. Liang, Y. Zhang, C. Ma, Z. Guo, X. Luo, H. Zhang, Two-dimensional tellurium: Progress, challenges, and prospects, Nano-Micro Lett. 12 (2020) 99, https://doi.org/10.1007/s40820-020-00427-z.
[31] W. Xu, L. Gan, R. Wang, X. Wu, H. Xu, Surface adsorption and vacancy in tuning the properties of tellurene, ACS Appl. Mater. Interfaces 12 (2020) 19110–19115, https://doi.org/10.1021/acsami.9b21625.
[32] L. Yu, D. Deng, X. Bao, Chain mail for catalysts, Angew. Chem., Int. Ed. 59 (2020) 15294–15297, https://doi.org/10.1002/anie.202007604.
[33] Y.C. Tu, H.B. Li, D.H. Deng, J.P. Xiao, X.J. Cui, D. Ding, M.S. Chen, X.H. Sao, Low charge overpotential of lithium-oxygen batteries with metallic co encapsulated in

single-layer graphene shell as the catalyst, Nano Energy 30 (2016) 877–884, https://doi.org/10.1016/j.nanoen.2016.08.066.
[34] D. Deng, L. Yu, X. Chen, G. Wang, L. Jin, X. Pan, J. Deng, G. Sun, X. Bao, Iron encapsulated within pod-like carbon nanotubes for oxygen reduction reaction, Angew. Chem. Int. Ed. 52 (2013) 371–375, https://doi.org/10.1002/anie.201204958.
[35] Y. Wang, H.-L. Fei, Improvement of a novel anode material TeO_2 by chlorine doping, Ionics 19 (2012) 771–776, https://doi.org/10.1007/s11581-012-0798-5.
[36] W.J. Yu, L.L. Zhang, P.X. Hou, F. Li, C. Liu, H.M. Cheng, High reversible lithium storage capacity and structural changes of Fe_2O_3 nanoparticles confined inside carbon nanotubes, Adv. Energy Mater. 6 (2016), 1501755, https://doi.org/10.1002/aenm.201501755.
[37] C. Kang, S. Zhou, J. Liu, Y. Zhu, A. Hu, Q. Tang, Y. Zhang, X. Chen, T. Tao, Confining sb nanoparticles in bamboo-like hierarchical porous aligned carbon nanotubes for use as an anode for sodium ion batteries with ultralong cycling performance, J. Mater. Chem. A 9 (2021) 2152–2160, https://doi.org/10.1039/d0ta10556b.
[38] L. Xu, Y.J. Hu, H.X. Zhang, H. Jiang, C.Z. Li, Confined synthesis of FeS_2 nanoparticles encapsulated in carbon nanotube hybrids for ultrastable lithium-ion batteries, ACS Sustain. Chem. Eng. 4 (2016) 4251–4255, https://doi.org/10.1021/acssuschemeng.6b00741.
[39] H. Tabassum, A. Mahmood, B. Zhu, Z. Liang, R. Zhong, S. Guo, R. Zou, Recent advances in confining metal-based nanoparticles into carbon nanotubes for electrochemical energy conversion and storage devices, Energy Environ. Sci. 12 (2019) 2924–2956, https://doi.org/10.1039/c9ee00315k.
[40] W.J. Yu, P.X. Hou, F. Li, C. Liu, Improved electrochemical performance of Fe_2O_3 nanoparticles confined in carbon nanotubes, J. Mater. Chem. 22 (2012) 13756–13763, https://doi.org/10.1039/c2jm31442h.
[41] W. Xing, J.R. Dahn, Study of irreversible capacities for Li insertion in hard and graphitic carbons, J. Electrochem. Soc. 144 (1997) 1195–1201, https://doi.org/10.1149/1.1837572.
[42] E. Buiel, J.R. Dahn, Li-insertion in hard carbon anode materials for Li-ion batteries, Electrochim. Acta 45 (1999) 121–130, https://doi.org/10.1016/s0013-4686(99)00198-x.
[43] Z. Liu, X.Y. Yu, U. Paik, Etching-in-a-box: a novel strategy to synthesize unique yolk-shelled Fe_3O_4@carbon with an ultralong cycling life for lithium storage, Adv. Energy Mater. 6 (2016), 1502318, https://doi.org/10.1002/aenm.201502318.
[44] S. Gayen, S.N. Behera, S.M. Bose, Raman spectra of unfilled and filled carbon nanotubes: theory, Phys. Rev. B 76 (2007), 165433, https://doi.org/10.1103/PhysRevB.76.165433.
[45] H. Wang, F. Liu, R. Yu, J. Wu, Unraveling the reaction mechanisms of electrode materials for sodium-ion and potassium-ion batteries by in situ transmission electron microscopy, Interdiscip. Mater. 1 (2022) 196–212, https://doi.org/10.1002/idm2.12008.
[46] P. Politzer, P. Lane, J.S. Murray, M.C. Concha, Comparative analysis of surface electrostatic potentials of carbon, boron/nitrogen and carbon/boron/nitrogen model nanotubes, J. Mol. Model. 11 (2005) 1–7, https://doi.org/10.1007/s00894-004-0202-0.

Shaoqing Rao is a Master candidate in School of Materials Science and Engineering at Wuhan University of Technology. His research interest focuses on the design of new type of energy conversion and storage devices.

Ruizhe Wu is currently an associate professor at Hubei University, School of Chemistry and Chemical Engineering. He received his B.S. degree in Chemistry from Nanjing University and Ph.D. degree in Chemical and Biological Engineering from Hong Kong University of Technology. His research interests focus on graphene-related composites and electrode materials in lithium metal batteries.

Zhu Zhu received her Bachelor degree from Jinan University in 2020. Now, she is a postgraduate at State Key Laboratory of Advanced Technology for Materials Synthesis and Processing and Nanostructure Research Centre in Wuhan University of Technology. Her research interests focus on electron microscopy and materials of batteries.

Jinsong Wu is currently a professor and executive director of Nanostructure Research Center at Wuhan University of Technology. He earned his Ph.D. degree from the Department of Materials Science and Engineering at Dalian University of Technology in 1998. He had worked in Juelich Research Center in Germany (1999–2001), Arizona State University (2001–2006), University of Georgia (2006–2007) and Northwestern University (2007–2018) in the USA as an electron microscopist. Dr. Wu's research interests include transmission electron microscopy, electron tomography, *in-situ* transmission electron microscopy and nanomaterials for energy storage.

Yao Ding is currently an associate professor at Wuhan University of Technology, School of Materials Science and Engineering. She earned her Master and Ph.D. degree from the Department of Chemical and Biological Engineering at Hong Kong University of Technology in 2018. Dr. Ding's research interests include the design of new type of energy conversion and storage devices, controllable synthesis of heterostructures based on semiconductors and their applications in energy conversion and storage.

Liqiang Mai is the Chair professor of Materials Science and Engineering at WUT, Dean of School of Materials Science and Engineering at WUT, Fellow of the Royal Society of Chemistry. He received his Ph.D. from WUT in 2004 and carried out his postdoctoral research at Georgia Institute of Technology in 2006–2007. He worked as an advanced research scholar at Harvard University and University of California, Berkeley. His current research interests focus on new nanomaterials for electrochemical energy storage and micro/nano energy devices.